KI REPORTS
KIReports.org

Deep Learning–Based Automated Imaging Classification of ADPKD

Youngwoo Kim[1], Seonah Bu[2], Cheng Tao[3] and Kyongtae T. Bae[4]; on behalf of the HALT Polycystic Kidney Disease Study Group[5]

[1]Department of Computer Software Engineering, Kumoh National Institute of Technology, Republic of Korea; [2]Jeju Technology Application Division, Korea Institute of Industrial Technology, Republic of Korea; [3]Department of Radiology, University of Pittsburgh Medical Center, Pittsburgh, Pennsylvania, USA; and [4]Department of Diagnostic Radiology, Li Ka Shing Faculty of Medicine, The University of Hong Kong, Pok Fu Lam, Hong Kong

Introduction: The Mayo imaging classification model (MICM) requires a prestep qualitative assessment to determine whether a patient is in class 1 (typical) or class 2 (atypical), where patients assigned to class 2 are excluded from the MICM application.

Methods: We developed a deep learning–based method to automatically classify class 1 and 2 from magnetic resonance (MR) images and provide classification confidence utilizing abdominal T_2-weighted MR images from 486 subjects, where transfer learning was applied. In addition, the explainable artificial intelligence (XAI) method was illustrated to enhance the explainability of the automated classification results. For performance evaluations, confusion matrices were generated, and receiver operating characteristic curves were drawn to measure the area under the curve.

Results: The proposed method showed excellent performance for the classification of class 1 (97.7%) and 2 (100%), where the combined test accuracy was 98.01%. The precision and recall for predicting class 1 were 1.00 and 0.98, respectively, with F_1-score of 0.99; whereas those for predicting class 2 were 0.87 and 1.00, respectively, with F_1-score of 0.93. The weighted averages of precision and recall were 0.98 and 0.98, respectively, showing the classification confidence scores whereas the XAI method well-highlighted contributing regions for the classification.

Conclusion: The proposed automated method can classify class 1 and 2 cases as accurately as the level of a human expert. This method may be a useful tool to facilitate clinical trials investigating different types of kidney morphology and for clinical management of patients with autosomal dominant polycystic kidney disease (ADPKD).

Kidney Int Rep (2024) **9,** 1802–1809; https://doi.org/10.1016/j.ekir.2024.04.002
KEYWORDS: atypical cyst; deep learning; explainable artificial intelligence; polycystic kidney disease; risk factors; total kidney volume

ADPKD is an inherited chronic kidney disease that may progress to severe kidney function impairment and is the fourth leading cause of end-stage kidney disease.[1-3] Appropriate clinical management of patients with ADPKD requires the accurate diagnosis and characterization of various factors that affect the growth of kidney cysts and progression of disease.[4] Several factors that are known to be strongly associated with the progression of ADPKD include patient's sex, age, kidney function, genotype, and total kidney volume (TKV). In particular, in a number of clinical investigations and trials, TKV has been the most widely utilized imaging biomarker to assess the severity of ADPKD and the risk to chronic kidney disease progression.[5,6]

Recently, with drastic advances in deep learning–based image processing techniques, various image analysis methods were proposed for automated segmentation of kidneys, kidney cysts, and liver in patients with ADPKD.[7-12] These advanced segmentation methods readily made the computation of highly reliable TKV measurements from computed tomography or MR images.

Once patient's height-adjusted TKV is computed, it can be used as an input variable along with patient's

Correspondence: Kyongtae T. Bae, Department of Diagnostic Radiology, Li Ka Shing Faculty of Medicine, The University of Hong Kong, 102 Pok Fu Lam Road, Hong Kong. E-mail: baekt@hku.hk

[5]Members of the HALT Polycystic Kidney Disease Study Group are listed in the Appendix.

Received 27 November 2023; revised 20 March 2024; accepted 1 April 2024; published online 4 April 2024

age to the MICM to assess the individual patient's risk for ADPKD progression.[13] The application of MICM, however, requires a prestep qualitative evaluation of the morphologic structure of kidney cysts and parenchyma to determine whether a patient is in class 1 (typical) or class 2 (atypical). Typically, 90% to 95% of the total population of patients with ADPKD are assigned into class 1 that are further classified into 5 subgroups (1A–1E) according to the MICM, where the division of the subgroups is strongly correlated with estimated glomerular filtration rate decrease.[13] Conversely, the remaining 5% to 10% of patients with ADPKD classified to be class 2 cannot be assessed with the MICM because their height-adjusted TKVs are weakly associated with estimated glomerular filtration rate.[14]

Although various methods were presented for the automated segmentation and measurement of TKV, no automated method has been reported for the image classification of class 1 and 2, which is currently performed manually and qualitatively by experts. We postulate that a deep learning–based automated method could be implemented to determine class 1 and 2 from MR imaging (MRI) images for the imaging classification of ADPKD.

Thus, the purpose of the study was to develop a deep learning–based automated procedure to classify class 1 and 2 from MR images in patients with ADPKD.

METHODS

Subjects, MRI, and Data Set

The subjects were from the HALT Polycystic Kidney Disease study, and we used HALT-A study only because HALT-B study did not include MRI.[15,16] The standardized MRI protocol was applied with 1.5 T MRI scanners for HALT-A study, and we exploited the coronal T_2-weighted single shot fast spin echo images with fat saturation in our study. The MRIs of the subjects were reviewed in consensus by ADPKD imaging experts following a set of image morphology criteria and classified into class 1 (typical) and class 2 (atypical). The details of the HALT Polycystic Kidney Disease study and the imaging classification criteria can be found in previous publications.[13,14]

A total of 486 subjects (245 male and 241 female) were selected from the HALT-A study. The parameters of the MR images were 59 to 176 μm per pixel resolution, 3 to 10 mm slice thickness, 60° to 180° flip angle, 3 to 24,806/1.5 to 122 ms repetition time/echo time, and average pixel resolution was 362.7 ± 117.6(H) × 362.7 ± 117.6(W) × 41.2 ± 16.2(D) with range of 256 to 640(H) × 256 to 640(W) × 16 to 204(D). The subjects were classified into typical ($n = 426$) and atypical ($n = 60$) cases with respect to the aforementioned imaging classification criteria, and the genetic background of the subjects classified as class 2 (atypical) is described in Table 1. Two radiologists, one with 25 years of experience in ADPKD imaging and the other with 20 years of experience in ADPKD imaging, were involved in the classification of the subjects into class 1 and 2. The representative MR images are depicted in Figure 1. The mean age of the typical and atypical subjects were 35.4 ± 8.4 years (range: 16–50 years) and 40.4 years ± 6.6 (range: 26–49 years), respectively.

The MR images from the 486 HALT-A subjects were further divided into 335 cases (including 295 typical and 40 atypical cases) for training and 151 cases (including 131 typical and 20 atypical) for testing the trained deep convolutional neural networks (DCNNs). Here, we observed a data imbalance between typical and atypical cases, where the number of atypical cases was fewer than that of typical cases. To mitigate the data imbalance, the atypical cases were composed of 3 exclusive data sets, where each data set contained 40 training and 20 testing cases, exclusively, resulting in 3 independent DCNN training sessions (TS_1, TS_2, and TS_3). The description of the data set is shown in Supplementary Figure S1.

Data Preprocessing

The MR images were normalized such that the image resolution and field of view used in the MR image acquisitions were adjusted to be consistent across the data set while preserving physical size of the kidneys. To this end, we used the ratio of the original voxel spacing (S_o) and the target voxel spacing (S_t), where S_t was set to 0.5 mm(H) × 0.5 mm(W) × 3 mm(D). The target resolutions were computed by multiplying original resolution and the ratio (S_o/S_t), and the original images were resized with the target resolutions, followed by the 3-dimensional zero padding enclosing the resized MR images to have a resolution of 1280(H) × 1280(W) × 204(D). Finally, a single representative midslice was selected whose location was at 65% of the

Table 1. Genetic background of subjects classified as class 2 (atypical) participated in this study

PKD1		PKD2				
Truncating	Nontruncating	Truncating	Nontruncating	NMD	Unknown	Total
13	16	11	3	8	9	60

NMD, no mutation detected; PKD, polycystic kidney disease.

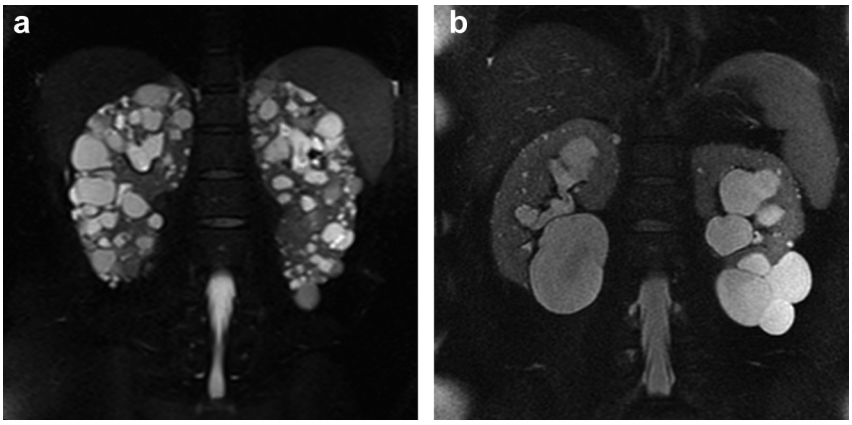

Figure 1. Exemplary MR images of class 1 and 2. (a) Class 1 example showing cysts of small to medium sizes distributed through parenchyma in bilateral kidneys, and (b) class 2 example showing a large dominant exophytic cyst in both kidneys and relatively asymmetric distribution of cysts in bilateral kidneys. MR, magnetic resonance.

distance spanning from the anterior to posterior edge of the MR images covering the kidneys (Figure 2). All the representative midslice images were examined, and the images were manually selected again if they did not include kidneys (typical) or exophytic cysts (atypical). The selected representative midslice images were augmented using color jitter, horizontal and vertical flip, rotation, and Gaussian blur.

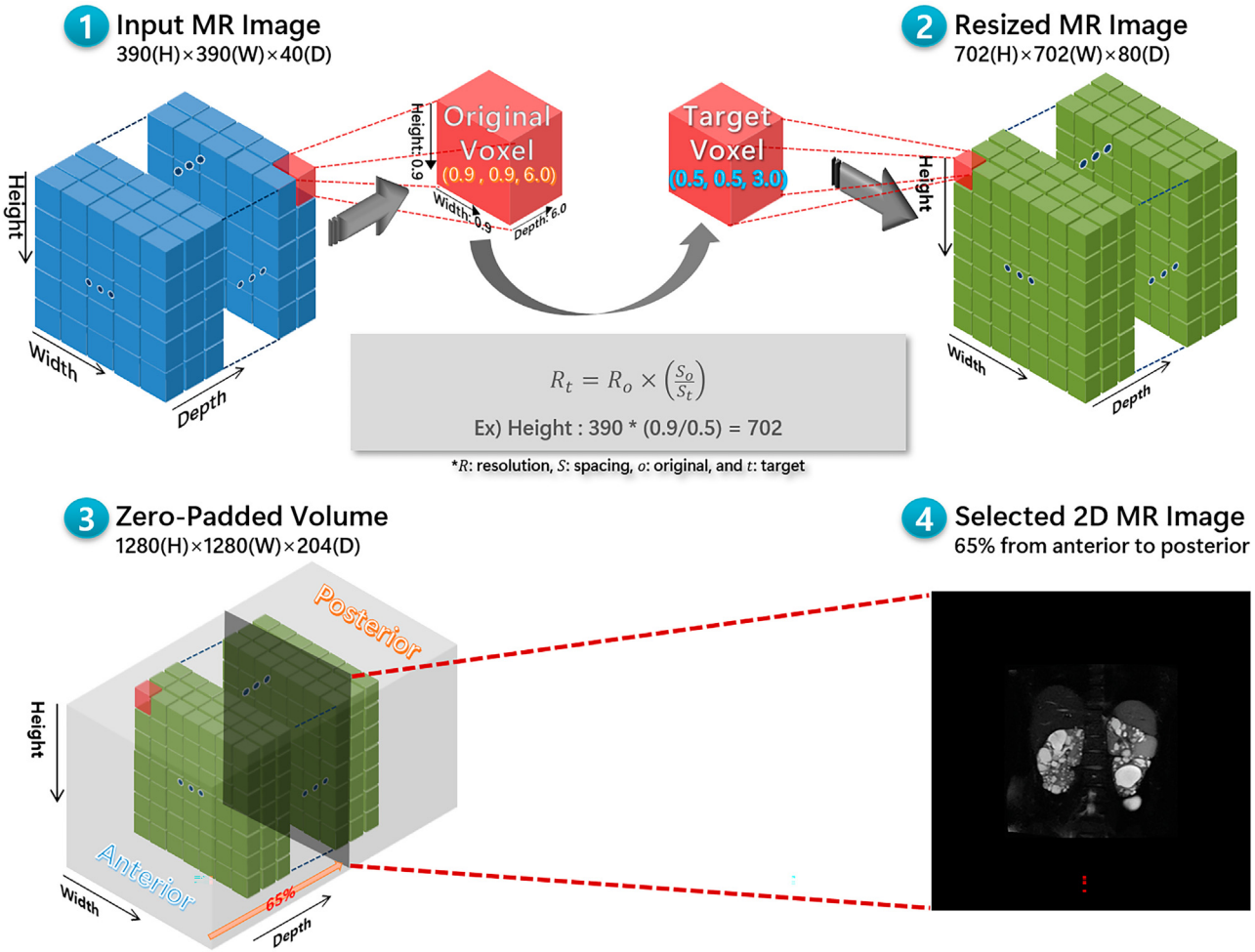

Figure 2. Pictorial illustration of the preprocessing of MR images. Input MR images are resized using the voxel spacing and slice thickness (depth) parameters. Zero padding is applied to the resized MR images. A single representative midslice image is selected at 65% of the distance spanning from the anterior to posterior edge of the MR images covering the kidneys. MR, magnetic resonance.

Deep Learning Architecture

The ResNet-50 (deep residual learning) architecture was initially adopted in our implementation for the classification of typical and atypical polycystic kidney disease, which is an extension of VGG-19 architecture by adding the residual blocks with skip connections.[17,18] The residual blocks enable ResNet-50 to have much deeper convolutional layers by passing information from the preceding convolutional layer, it can effectively optimize the DCNN with a superior accuracy. In our implementation, the first 2 convolutional layers were frozen for the transfer learning by using pretrained weights trained with the ImageNet-1K data set.[19] Stochastic gradient descent algorithm and a cross-entropy were utilized for an optimization of DCNN and evaluation metrics, respectively, and the epoch was set to 1000. The ResNet-50 architecture was built with Python (v3.8.5; Wilmington, DE), PyTorch framework (v1.7.1),[20] and Ubuntu 16.04 LTS (Canonical Ltd, London, UK). The data preparation, preprocessing, training, and testing for the automated classification algorithm were performed using the hardware equipped with Intel Xeon Gold 6252 central processing unit, 1 Nvidia Titan RTX graphics processing unit, and 128GB random-access memory.

Classification Confidence and XAI

Considering that the DCNN model predicts the imaging class, it can also provide quantitative classification confidence in each prediction. In the DCNN architecture, we applied the softmax function to the output, and chose the class with a higher value that was informed as the diagnostic confidence.[21]

In order to aid the explainability of the automated classification, the DCNN models were analyzed using the XAI technique that extracts regions highly contributory to the decision of the automated classification. In our implementation, the local interpretable model-agnostic explanations algorithm was adopted, which is most widely utilized for XAI in the literature.[22] The algorithm first segmented an input image into superpixels in that the segments of high prediction accuracy were highlighted for their significance in the contribution to the classification. The simple linear iterative clustering method was employed to segment the input image into superpixels, where the number of superpixels and the compactness parameters were set to 200 and 10, respectively.[23] The visual illustration of applying the simple linear iterative clustering and the local interpretable model-agnostic explanations algorithm is presented in Figure 3.

Statistical Analysis

To evaluate the performance of the automated classification of typical and atypical polycystic kidney disease, we compared the automated classification output with the reference standard from the HALT-A study. First, the confusion matrices were generated based on the automated classification output, and the metrics to examine the accuracy, including precision, recall, and F_1-score, were derived. Second, receiver operating characteristic curves were drawn to measure the area under the curve. The statistical analyses were conducted using the scikit-learn (v1.0.2) and Pandas (v1.2.4) packages.[24,25]

RESULTS

Each of the 3 DCNN models (TS_1, TS_2, and TS_3) correctly predicted 20 out of the 20 test MR images for the atypical cases (100%) and 128 out of the 131 test MR images for the typical cases (97.7%), thus the combined test accuracy of 98.01%. The precision and recall for predicting the atypical cases were 0.87 and

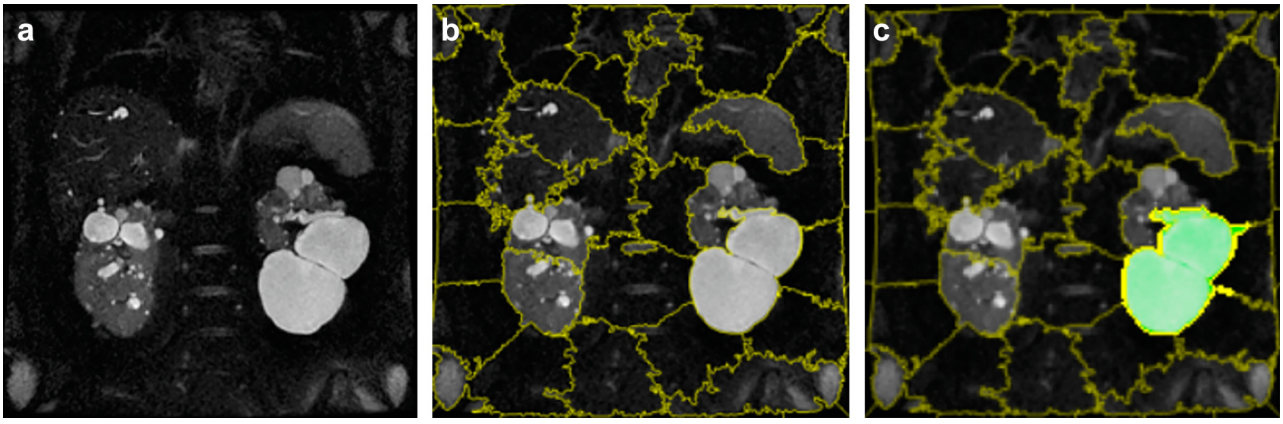

Figure 3. Visual illustration of the explainable artificial intelligence procedure: (a) original input MR image, (b) application of simple linear iterative clustering algorithm segmenting the input MR image into superpixels where yellow lines represent boundaries of superpixels, and (c) application of local interpretable model-agnostic explanations algorithm that highlights (in green color) the superpixels contributing greatly to the automated classification. MR, magnetic resonance.

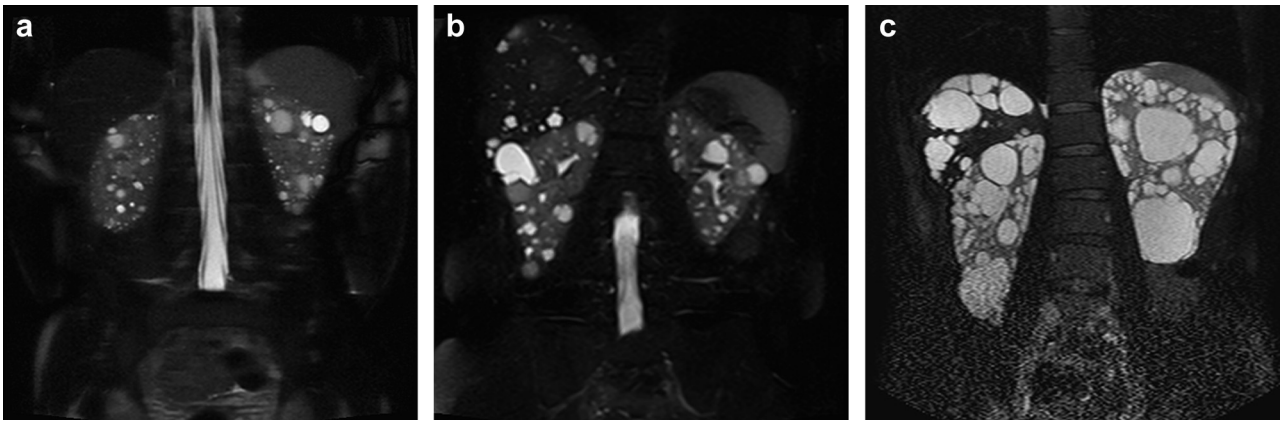

Figure 4. Three typical cases correctly classified by the DCNN model but with relatively lower probabilities for the typical classification. The probability for the typical classification was (a) 93.0%, (b) 69.8%, and (c) 55.7%, respectively, which was lower than 99% for those of the most of the correctly classified typical cases. DCNN, deep convolutional neural network.

1.00, respectively, with the F_1-score of 0.93. The precision and recall for predicting the typical cases were 1.00 and 0.98, respectively, with the F_1-score of 0.99. The macro averages of precision and recall were 0.93 and 0.99, respectively, and the weighted averages of precision and recall were 0.98 and 0.98, respectively. The macro average and the weighted average of the F_1-score were 0.96 and 0.98, respectively. The confusion matrix is shown in Supplementary Figure S2A. The area under the curve of the receiver operating characteristic curve in Supplementary Figure S2B was 0.988. The 3 DCNN models were identical in their confusion matrices and receiver operating characteristic curves.

The 128 typical cases that were correctly classified out of 131 typical cases showed the probabilities ranging from 55.7% to 100%. Of the 128 correctly classified typical cases, 4 had relatively low probabilities for the typical classification (93.0%, 82.9%, 69.8%, and 55.7%), whereas the remaining 124 cases had their probabilities greater than 99%. In Figure 4, we illustrate example MR images with relatively low probabilities for the typical classification. The 2 cases in Figure 4a and b show mild burden of scattered intraparenchymal cysts that may limit a precise characterization of cyst morphology in the kidneys. The case in Figure 4c presents with several large dominant cysts in the kidneys that are borderline features in determining cyst morphology.

The 3 typical cases that were misclassified by the DCNN models to be atypical are shown in Figure 5. Their probabilities to be typical were 11.8%, 1.9%, and 1.6%, respectively. The case in Figure 5a may be misclassified because of a dominant and several small exophytic cysts in the left kidney. The misclassification of the 2 cases in Figure 5b and c may be attributed to their large dominant cysts occupying the kidney parenchyma that were also covered by other numerous small cysts.

In Figure 6, we show several exemplary atypical cases that graphically illustrate the relative contributions of various image features to the classification outcomes of the models. Each column represents an image pair with the original MR image and the corresponding local interpretable model-agnostic explanations results. The boundaries of the superpixels using the simple linear iterative clustering method are drawn in yellow color, whereas the superpixels contributing greatly to the classification are superimposed in green color. The XAI technique depicts the regions of contribution that may explain the classification outcome. In these examples of atypical cases, the highlighted superpixels included larger areas for the dominant exophytic cysts that signify the key morphology features of the atypical classification.

DISCUSSION

The MICM has been widely used as a risk prediction model in clinical management and trials for patients with ADPKD since its inception. Although the use of the MICM is relatively straightforward requiring only 2 input parameters (patient's age and height-adjusted TKV), the user should predetermine whether the patient is of the typical or atypical morphology in kidneys. Specifically, subgroups of typical cases (i.e., class 1A–1E) are well-associated with estimated glomerular filtration rate decrease, whereas atypical cases (class 2) are ruled out from the model because height-adjusted TKV of these cases do not predict well the risk of ADPKD progression. Therefore, the qualitative assessment to classify whether a test case is typical or atypical is mandatory before the use of the MICM.

The classification of class 1 and 2 requires a careful evaluation of morphology of kidneys from computed

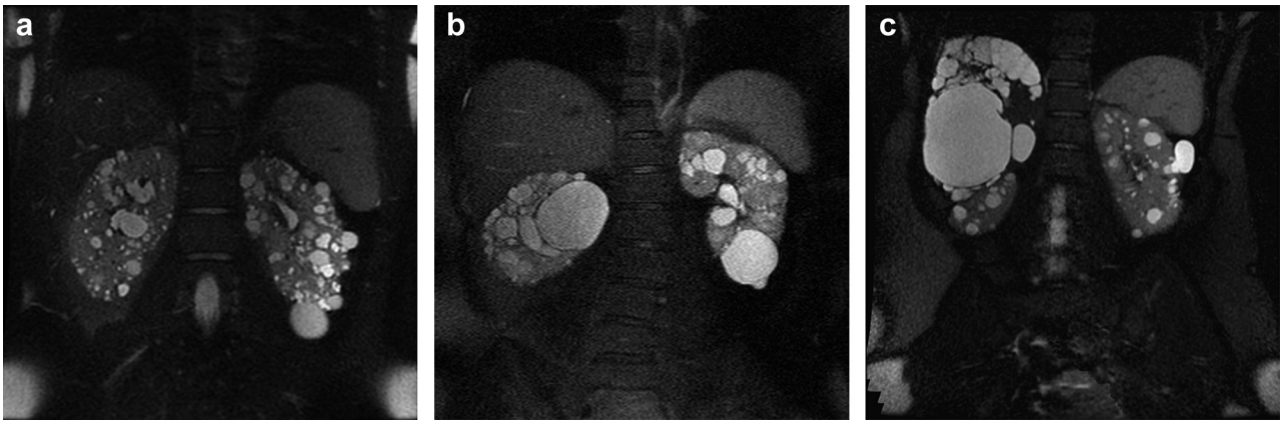

Figure 5. Three typical cases misclassified to be atypical class by the DCNN model. The probability for the typical classification was (a) 11.8%, (b) 1.9%, and (c) 1.6%, respectively, which was much lower than 99% for those of the most of the correctly classified typical cases. DCNN, deep convolutional neural network.

tomography or MR images following the published cyst morphology classification criteria.[13,14] An alternative approach is to use a fully automated software to segment kidneys and exophytic cysts as proposed by Kim *et al*.[10] This software, however, may not be readily available given the requirements of hardware equipment, including high performance graphics processing unit cards, central processing units, and random access memories. Furthermore, the processing time of this software exponentially increases with moderate or even low hardware equipment using only central processing units.

In the current study, we proposed a fully automated triage with a light-weight and fast processing by selecting a representative 2D slice, which can be an effective and efficient methodology when clinicians apply the automated segmentation method to only automatically classified atypical cases with the proposed triage and exclude prominent exophytic cysts so that the atypical case can be analyzed using the MICM. The source code and trained model weights are available online at https://github.com/ywkim0909/XAI-ADPKD-Net.

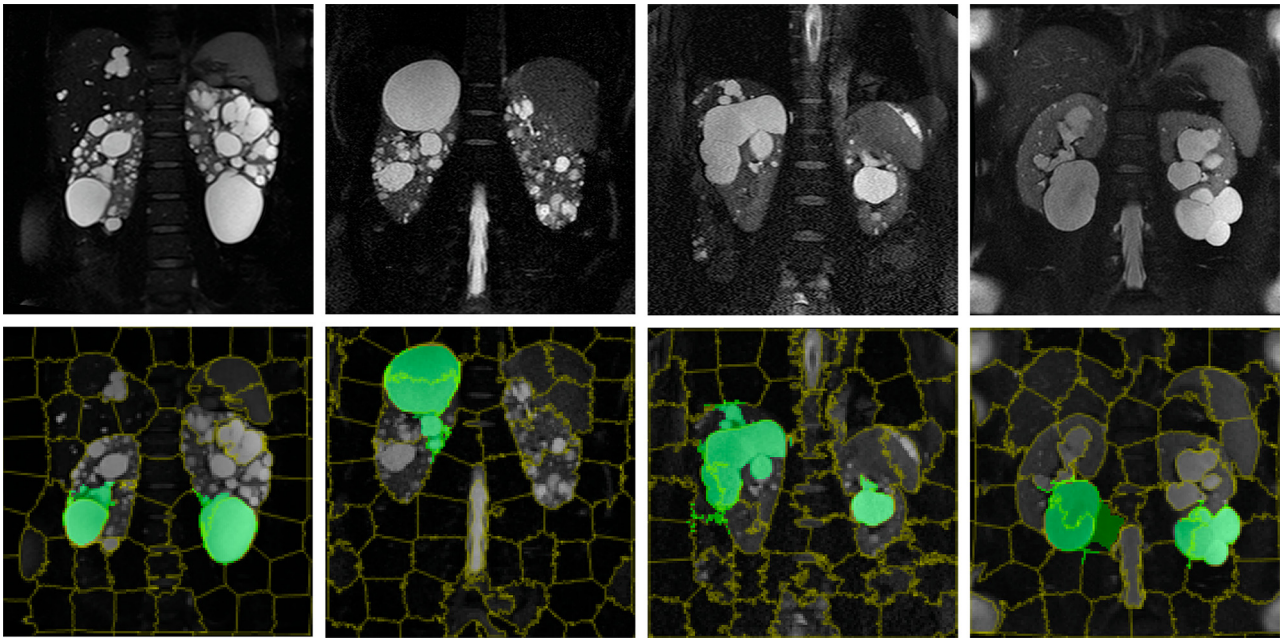

Figure 6. XAI technique illustrating how image features contribute to the classification outcomes in these examples of atypical cases. The DCNN models were analyzed using the LIME technique, which is one of XAI techniques, and the regions are superimposed in green color that most highly contributed to the process of the decision making. Each column represents the original MR image (top row) and the contributory superpixels (bottom row) that are superimposed in green color whereas the boundaries of the superpixels are drawn in yellow lines. DCNN, deep convolutional neural network; LIME, local interpretable model-agnostic explanations; MR, magnetic resonance; XAI, explainable artificial intelligence.

To the best of our knowledge, our proposed approach is the first automated method to classify the MR images from a patient with ADPKD into typical or atypical. The experimental results showed 98.01% classification accuracy, where the accuracy for atypical and typical case classifications were 100% and 97.7%, respectively. Out of 151 test cases (131 typical and 20 atypical cases), only 3 typical cases from typical cases were classified as atypical to which the automated kidneys and exophytic cysts segmentation method to small portion merely small portion (5%–10%). The misclassified cases show either relative paucity of kidney cysts or some prominent cysts adjacent to boundaries of renal parenchyma that may lead to a borderline classification. This implies that it is feasible to apply the automated kidneys and exophytic cysts segmentation method to merely atypical and the misclassified cases, which may alleviate the computational burden for disease management and clinical trials. Although our study has a limitation in that the number of training and test sets of atypical cases were relatively small, we utilized the separate and independent 3 training and test sets and evaluated that the proposed method performed well on the test sets.

Our proposed method also provides a classification confidence using a quantitative value to indicate whether a test case is confidently classified or on the borderline between typical and atypical. The classification confidence level can be useful in the circumstances when clinicians need to explain a basis in terms of a classification with a highlighted area in an MR image deduced by XAI. The highlighted region may slightly overestimate potential areas of contribution, but it could be negligible because the purpose of applying XAI was to notify the contribution regions rather than accurately segment boundaries.

In conclusion, we developed a fully automated method to classify MR images from a patient with ADPKD into typical or atypical for the MICM. Our method can also provide a quantitative classification confidence level and graphical illustration of highlighted areas contributing to the classification decision based on the XAI technology. This novel tool may facilitate clinical trials investigating different types of kidney morphology and clinical management of patients with ADPKD.

APPENDIX

List of the HALT Polycystic Kidney Disease Study Group

Theodore Steinman, Jesse Wei, Peter Czarnecki, Ivan Pedrosa, William Braun, Saul Nurko, Erick Remer, Arlene Chapman, Diego Martin, Frederic Rahbari-Oskoui, Pardeep Mittal, Vicente Torres, Marie C. Hogan, Ziad El-Zoghby, Peter Harris, James Glockner, Bernard King Jr., Ronald Perrone, Neil Halin, Dana Miskulin, Robert Schrier, Godela Brosnahan, Berenice Gitomer, Cass Kelleher, Amirali Masoumi, Nayana Patel, Franz Winklhofer, Jared Grantham, Alan Yu, Connie Wang, Louis Wetzel, Charity G. Moore, James E. Bost, Kyongtae Bae, Kaleab Z. Abebe, J. Philip Miller, Paul A. Thompson, Josephine Briggs, Michael Flessner, Catherine M. Meyers, Robert Star, James Shayman, William Henrich, Tom Greene, Mary Leonard, Peter McCullough, Sharon Moe, Michael Rocco, David Wendler.

DISCLOSURE

All the authors declared no competing interests.

ACKNOWLEDGMENTS

This study has been conducted with the support of the Korea Institute of Industrial Technology as “Development of core technology for smart wellness care based on cleaner production process technology (Kitech-PEH23030)”.

DATA AVAILABILITY STATEMENT

Sharing of data related to this study would be a violation of Health Insurance Portability and Accountability Act and policies provided by our institutional review board.

AUTHOR CONTRIBUTIONS

YK and KTB designed the study. YK, CT, and KTB acquired clinical and imaging data. YK, SB, and KTB analyzed the data. YK and SB made the figures. YK and KTB drafted the manuscript. All the authors reviewed, revised, and approved the final version of the manuscript.

SUPPLEMENTARY MATERIAL

Supplementary File (PDF)

Figure S1. Data set flowchart showing the number and distribution of participants.

Figure S2. Plot depicting the performance of the automated classification using confusion matrix and receiver operating characteristic curve.

REFERENCES

1. Gabow PA. Autosomal dominant polycystic kidney disease. *N Engl J Med*. 1993;329:332–342. https://doi.org/10.1056/NEJM199307293290508
2. Ong ACM, Devuyst O, Knebelmann B, Walz G, ERA-EDTA Working Group for Inherited Kidney Diseases. Autosomal dominant polycystic kidney disease: the changing face of clinical management. *Lancet (Lond Engl)*. 2015;385:1993–2002. https://doi.org/10.1016/S0140-6736(15)60907-2
3. Chapman AB, Guay-Woodford LM, Grantham JJ, et al. Renal structure in early autosomal-dominant polycystic kidney

disease (ADPKD): the Consortium for Radiologic Imaging Studies of Polycystic Kidney Disease (CRISP) cohort 1. *Kidney Int*. 2003;64:1035–1045. https://doi.org/10.1046/j.1523-1755.2003.00185.x

4. Chebib FT, Torres VE. Recent advances in the management of autosomal dominant polycystic kidney disease. *Clin J Am Soc Nephrol*. 2018;13:1765–1776. https://doi.org/10.2215/CJN.03960318
5. Alam A, Dahl NK, Lipschutz JH, et al. Total kidney volume in autosomal dominant polycystic kidney disease: a biomarker of disease progression and therapeutic efficacy. *Am J Kidney Dis*. 2015;66:564–576. https://doi.org/10.1053/j.ajkd.2015.01.030
6. Xue C, Zhou C, Mei C. Total kidney volume: the most valuable predictor of autosomal dominant polycystic kidney disease progression. *Kidney Int*. 2018;93:540–542. https://doi.org/10.1016/j.kint.2017.10.027
7. Kim Y, Bae SK, Cheng T, et al. Automated segmentation of liver and liver cysts from bounded abdominal MR images in patients with autosomal dominant polycystic kidney disease. *Phys Med Biol*. 2016;61:7864–7880. https://doi.org/10.1088/0031-9155/61/22/7864
8. Sharma K, Rupprecht C, Caroli A, et al. Automatic segmentation of kidneys using deep learning for total kidney volume quantification in autosomal dominant polycystic kidney disease. *Sci Rep*. 2017;7:2049. https://doi.org/10.1038/s41598-017-01779-0
9. Gregory AV, Anaam DA, Vercnocke AJ, et al. Semantic instance segmentation of kidney cysts in MR images: a fully automated 3D approach developed through active learning. *J Digit Imaging*. 2021;34:773–787. https://doi.org/10.1007/s10278-021-00452-3
10. Kim Y, Tao C, Kim H, Oh G-Y, Ko J, Bae KT. A deep learning approach for automated segmentation of kidneys and exophytic cysts in individuals with autosomal dominant polycystic kidney disease. *J Am Soc Nephrol*. 2022;33:1581–1589. https://doi.org/10.1681/ASN.2021111400
11. Goel A, Shih G, Riyahi S, et al. Deployed deep learning kidney segmentation for polycystic kidney disease MRI. *Radiol Artif Intell*. 2022;4:e210205. https://doi.org/10.1148/ryai.210205
12. Zhao D, Wang W, Tang T, Zhang Y-Y, Yu C. Current progress in artificial intelligence-assisted medical image analysis for chronic kidney disease: a literature review. *Comput Struct Biotechnol J*. 2023;21:3315–3326. https://doi.org/10.1016/j.csbj.2023.05.029
13. Irazabal MV, Rangel LJ, Bergstralh EJ, et al. Imaging classification of autosomal dominant polycystic kidney disease: a simple model for selecting patients for clinical trials. *J Am Soc Nephrol*. 2015;26:160–172. https://doi.org/10.1681/ASN.2013101138
14. Irazabal MV, Abebe KZ, Bae KT, et al. Prognostic enrichment design in clinical trials for autosomal dominant polycystic kidney disease: the HALT-PKD clinical trial. *Nephrol Dial Transplant*. 2017;32:1857–1865. https://doi.org/10.1093/ndt/gfw294
15. Chapman AB, Torres VE, Perrone RD, et al. The HALT polycystic kidney disease trials: design and implementation. *Clin J Am Soc Nephrol*. 2010;5:102–109. https://doi.org/10.2215/CJN.04310709
16. Schrier RW, Abebe KZ, Perrone RD, et al. Blood pressure in early autosomal dominant polycystic kidney disease. *N Engl J Med*. 2014;371:2255–2266. https://doi.org/10.1056/NEJMoa1402685
17. Simonyan K, Zisserman A. Very deep convolutional networks for large-scale image recognition. Preprint. Posted online September 4, 2014. ArXiv: 1409.1556v6. https://doi.org/10.48550/arXiv.1409.1556
18. He K, Zhang X, Ren S, Sun J. Deep residual learning for image recognition. Paper presented at: 2016 IEEE Conference on Computer Vision and Pattern Recognition (CVPR); June 27-30, 2016; Las Vegas, NV.
19. Russakovsky O, Deng J, Su H, et al. ImageNet large scale visual recognition challenge. *Int J Comput Vis*. 2015;115:211–252. https://doi.org/10.1007/s11263-015-0816-y
20. Paszke A, Gross S, Massa F, et al. PyTorch: an imperative style, high-performance deep learning library. In: Wallach H, Larochelle H, Beygelzimer A, et al., eds. Advances in Neural Information Processing Systems 32 (NeurIPS 2019). 2019:8026–8037. Proceedings of the 33rd International Conference on Neural Information Processing Systems (NeurIPS 2019), Vancouver, Canada.
21. Sensoy M, Kaplan L, Kandemir M. Evidential deep learning to quantify classification uncertainty. In: *Proceedings of the 32nd International Conference on Neural Information Processing Systems*. Curran Associates Inc.; 2018:3183–3193.
22. Ribeiro M, Singh S, Guestrin C. "Why Should I Trust You?": explaining the predictions of any classifier. In: *Proceedings of the 2016 Conference of the North American Chapter of the Association for Computational Linguistics: Demonstrations*. Association for Computational Linguistics; 2016:97–101. https://doi.org/10.18653/v1/N16-3020
23. Achanta R, Shaji A, Smith K, Lucchi A, Fua P, Süsstrunk S. SLIC superpixels compared to state-of-the-art superpixel methods. *IEEE Trans Pattern Anal Mach Intell*. 2012;34:2274–2282. https://doi.org/10.1109/TPAMI.2012.120
24. Pedregosa F, Varoquaux G, Gramfort A, et al. Scikit-learn: machine learning in python. *J Mach Learn Res*. 2011;12:2825–2830.
25. McKinney W. Data structures for statistical computing in python. In: *Proceedings of the Python in Science Conference*. Proceedings of the 9th Python in Science Conference; 2010: 51–56. https://doi.org/10.25080/Majora-92bf1922-00a